JPP JOURNAL OF Pharmacy and Pharmacology
ROYAL PHARMACEUTICAL SOCIETY
JPP Journal of Pharmacy And Pharmacology
Research Paper

Exploring the biotransformation of *N*-(2-hydroxyphenyl)-2-propylpentanamide (an aryl valproic acid derivative) by CYP2C11, using *in silico* predictions and *in vitro* studies

Jessica Elena Mendieta-Wejebe[a], Arianna Silva-Trujillo[a], Martiniano Bello[b], Humberto L. Mendoza-Figueroa[b], Norma Lizeth Galindo-Alvarez[b], Arnulfo Albores[c], Feliciano Tamay-Cach[d], Martha Cecilia Rosales-Hernández[a], Aurelio Romero-Castro[e] and José Correa-Basurto[b]

[a]Laboratorio de Biofísica y Biocatálisis, [b]Laboratorio de Diseño y Desarrollo de Nuevos Fármacos e Innovación Biotecnológica (Laboratory for the Design and Development of New Drugs and Biotechnological Innovation), Escuela Superior de Medicina, [c]Sección de Toxicología, Centro de Investigación y de Estudios Avanzados, [d]Laboratorio de Investigación Bioquímica, Escuela Superior de Medicina, Instituto Politécnico Nacional, Ciudad de México and [e]División de Ciencias de la Salud, Universidad de Quintana Roo, Chetumal, México

Keywords
CYP2C11; HO-AAVPA; rat liver microsomes; valproic acid

Correspondence
Jessica Elena Mendieta-Wejebe, Laboratorio de Biofísica y Biocatálisis, Escuela Superior de Medicina, Instituto Politécnico Nacional, Plan de San Luis y Salvador Díaz Mirón s/n, Casco de Santo Tomás, Ciudad de México 11340, México.
E-mail: jesmenwej@yahoo.com
José Correa Basurto, Laboratorio de Diseño y Desarrollo de Nuevos Fármacos e Innovación Biotecnológica (Laboratory for the Design and Development of New Drugs and Biotechnological Innovation), Escuela Superior de Medicina, Instituto Politécnico Nacional, Plan de San Luis y Salvador Díaz Mirón, Ciudad de México 11340, México.
E-mail: corrjose@gmail.com

Received January 6, 2020
Accepted March 21, 2020

doi: 10.1111/jphp.13270

Abstract

Objectives *N*-(2-hydroxyphenyl)-2-propylpentanamide (HO-AAVPA), a derivative of valproic acid (VPA), has been proposed as a potential anticancer agent due to its improved antiproliferative effects in some cancer cell lines. Although there is evidence that VPA is metabolized by cytochrome P450 2C11 rat isoform, HO-AAVPA CYP-mediated metabolism has not yet been fully explored. Therefore, in this work, the biotransformation of HO-AAVPA by CYP2C11 was investigated.

Methods Kinetic parameters and spectral interaction between HO-AAVPA and CYP were evaluated using rat liver microsomes. The participation of CYP2C11 in metabolism of HO-AAVPA was confirmed by cimetidine (CIM) inhibition assay. Docking and molecular dynamics simulations coupled to MMGBSA methods were used in theoretical study.

Key findings HO-AAVPA is metabolized by CYP enzymes (K_M = 38.94 μM), yielding a hydroxylated metabolite according to its HPLC retention time (5.4 min) and MS analysis (252.2 m/z). In addition, CIM inhibition in rat liver microsomes (K_i = 59.23 μM) confirmed that CYP2C11 is mainly involved in HO-AAVPA metabolism. Furthermore, HO-AAVPA interacts with CYP2C11 as a type I ligand. HO-AAVPA is stabilized at the CYP2C11 ligand recognition site through a map of interactions similar to other typical CYP2C11 substrates.

Conclusion Therefore, rat liver CYP2C11 isoform is able to metabolize HO-AAVPA.

Introduction

Cancer is a major disease that affects millions of people worldwide. Current treatments are usually complex, and some are highly toxic, causing several side effects.[1] Hence, the development of therapeutic alternatives with lower toxicity has become a priority. Valproic acid (VPA) has been used for the treatment of some types of cancer, including haematologic malignancies.[2] However, some studies have demonstrated that VPA is hepatotoxic due to its reactive metabolites 4-ene-valproic acid (4-ene-VPA) and 2,4-diene-valproic acid (2,4-diene-VPA), which are enzymatically generated by cytochrome P-450 (CYP). Moreover, VPA metabolism induces hepatocyte membrane lysis and ROS formation.[3,4] Therefore, *N*-(2-hydroxyphenyl)-2-propylpentanamide (HO-AAVPA; Scheme 1), an aryl derivative of VPA, has been proposed from theoretical studies by our research group.[5] HO-AAVPA could be a potential

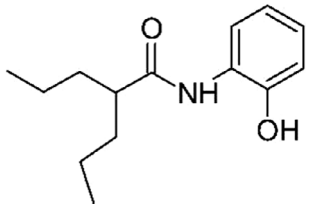

Scheme 1 Chemical structure of *N*-(2-hydroxyphenyl)-2-propylpentanamide (HO-AAVPA).

anticancer agent due to its antiproliferative effects in some cancer cell lines, such as cervical cancer (HeLa), undifferentiated sarcoma (A204) and some breast cancer cells.[5] In these assays, it was shown that HO-AAVPA has a higher antiproliferative effect than VPA (patent: MX 363005 B).[5]

The enzymatic (metabolic) stability assessment of a new drug is an essential step in the early stages of its development since the optimization of its pharmacokinetic properties is very important for continuation of the pharmacological evaluation. Hepatic metabolism is the main pathway for drug elimination, where cytochrome (CYP) enzymes, which are located in the hepatocyte endoplasmic reticulum, play a major role. The stages of CYP catalysis inherently involve the binding of the substrate to the active site, causing a change in the redox potential of the ferric ion (Fe^{3+}) in the haem group, triggering a series of complex oxidation reactions: hydroxylation, formation of C–C bonds and cleavage of the corresponding substrate, among others.[6] It has been demonstrated that CYP2C9 is one of the main isoforms involved in drug biotransformation in humans.[7] Additionally, it is well known that rat CYP homolog models can be used for human metabolism studies.[8] It has been found that the best homolog of the human isoform CYP2C9 in rats is CYP2C11.[9] CYP2C11 is approximately 50% of the total CYP isoform content in the rat liver microsomal system and is responsible for the hydroxylation of testosterone at the 2-α and 16-α positions,[10] as well as VPA metabolism.[9] In addition, CYP enzymes are susceptible to induction or inhibition by several xenobiotics, leading to drug–drug interactions when they are coadministered.[11] For example, it has been demonstrated that low concentrations of dexamethasone (DEX) induce the expression of CYP2C11,[12] whereas cimetidine (CIM) is a specific CYP2C11 inhibitor.[13,14]

CYP enzymes bind multiple substrates by two interaction modes known as type I and type II, which have been extensively studied using ultraviolet-visible (UV-Vis) spectrophotometry. Type I ligands are characterized by the appearance of an absorbance minimum at 420 nm and a peak at 385–390 nm, whereas the type II ligands show an absorption peak at approximately 430 nm and a minimum at 390 nm.[15]

Thus, due to the promising application of HO-AAVPA in cancer therapy, this study aimed to investigate its metabolism by the CYP2C11 isoform. Experimentally, the HO-AAVPA metabolic profile was assessed using rat liver microsomes, and the obtained metabolites were analysed by liquid chromatography coupled to mass spectrometry (LC-MS). Interaction modes and binding free energy values between the HO-AAVPA and CYP2C11 isoforms were evaluated by docking and molecular dynamics (MD) simulations with the molecular mechanics generalized-born surface area (MMGBSA) approach. Finally, two HO-AAVPA metabolites were synthesized to be compared with those obtained from rat liver microsomes and those predicted by the *in silico* methods.

Materials and Methods

Animals

Male rats of the Sprague-Dawley strain (180 ± 20 g) were obtained from Harlan Laboratories (Indianapolis, IN, USA). One week before the experimental assays, animals were allowed to acclimatize and fed with rat chow and drinking water *ad libitum* during this period. Animals were divided into two groups: Group I (n = 5), without treatment; and Group II (n = 5), treated with an intraperitoneal (i.p.) injection of DEX (40 mg/kg per day).[16] At the end of the experimental, animals were euthanized using pentobarbital, immediately after which the livers were rapidly removed and placed on ice for microsomal preparation. All procedures described in this study were conducted in accordance with the Mexican Official Standard NOM-062-ZOO-1999, Technical Specifications for Production, Care and Use of Laboratory Animals. Furthermore, the protocol was approved by the Ethics Committee for the Care and Use of Laboratory Animals (Approval number: ESM.CICUAL-02/27-07-2015) of the Escuela Superior de Medicina-IPN (http://www.sepi.esm.ipn.mx/Paginas/CICUAL.aspx).

Reagents and standards

Glucose 6-phosphate (G6P), glucose 6-phosphate dehydrogenase (G6PDH), magnesium chloride ($MgCl_2.6H_2O$), β-nicotinamide adenine dinucleotide phosphate ($NADP^+$), (−)-nicotine hydrogen tartrate salt, diclofenac sodium salt, DEX, CIM, estradiol, dimethyl sulfoxide (DMSO) and acetic acid ($C_2H_4O_2$) were reagent grade, while the acetonitrile (ACN) and the deionized water used were HPLC grade. All reagents and solvents were purchased from Sigma-Aldrich (St Louis, Mo, USA). HO-AAVPA was synthesized in our laboratory,[5] and its purity was >97%, as confirmed by high-performance liquid chromatography (HPLC; Agilent infinity 1260) analysis. Its authenticity was

determined using mass spectrometry (MS), nuclear magnetic resonance (NMR, ^{1}H and ^{13}C) and Fourier transform infrared (FTIR) spectroscopies. These analyses were performed at the Centro de Nanociencias y Micro-Nanotecnología-IPN (https://www.ipn.mx/nanocentro/).

Microsomal preparations

Rat liver microsomes were prepared according to the method described by Manno *et al.*[17] Samples were stored in 0.1 M phosphate buffer, pH 7.4 with 20% glycerol at −80°C until use. The protein concentration in the microsomal preparation was determined with the commercial Bradford kit (Protein Determination Kit, Item No. 704002, Cayman Chemical). The CYP content was estimated following the method used by Omura and Sato, 1964.[15]

HO-AAVPA metabolism by rat liver microsomal CYP enzymes

Rat liver microsomes (300 μg of protein in 0.1 M phosphate buffer, pH 7.4) for both DEX-induced and non-induced microsomes were incubated in a 96-well plate at different concentrations of HO-AAVPA dissolved in ACN (5, 10, 20, 50, 100 and 250 μM). All samples were run in triplicate. Plates were placed in a water bath at 37°C. Diclofenac was used as the reference substrate for CYP2C11.[18] The reaction was initiated by the addition of a solution of NADPH regenerating system (1.3 mM $NADP^{+}$, 3.3 mM G6P, 0.4 U G6PDH and 3.3 mM $MgCl_2$).[19] With the purpose of excluding potential factors that could interfere in the reaction, the controls used were (1) solution buffer only, (2) solution buffer containing microsomes only and (3) solution buffer containing the reaction mix without the NADPH regenerating system. The reactions were quenched with 0.6 ml of ice-cold ACN after 0, 5, 15, 25, 35 or 45 min. Samples were vortexed and then centrifuged at 6940 *g* for 10 min in a Hettich 320 R centrifuge (Hettich, Germany). Subsequently, the supernatant was removed and filtered, and a 10 μL aliquot was injected into the HPLC instrument (Agilent 1260 Infinity Series; Agilent Technologies, Palo Alto, CA, USA) for immediate analysis. The mobile phase consisted of a mixture of A) 0.2% acetic acid in water (v/v) and B) ACN, in a proportion of 40% A and 60% B. HPLC analysis was performed with isocratic elution and a flow rate of 0.5 ml/min. The stationary phase was a Zorbax SB-C18 column (5 μm, 4.6 × 150 mm) at a temperature of 25°C. UV detection was measured at 242 nm.[20]

All graphs were constructed using GraphPad Prism version 5.01 software (GraphPad Software, San Diego, CA, USA). The depletion constant (k_dep) was estimated at different compound concentrations with linear regression analysis, according to the first-order equation $C = C_0(e^{-k\_dept})$. The Michaelis–Menten parameters (V_{max} and K_M) were determined based on the non-linear regression of the plot obtained from the product formation velocity vs the substrate concentration using the Obach–Reed–Hagen equation: $k\_dep = k\_dep_{([S]\rightarrow 0)}[1-([S]/[S] + K_M)]$, where [S] is the substrate concentration. The V_{max} was calculated based on the equation $k\_dep_{([S]\rightarrow 0)} = V_{max}/K_M$.[21]

Inhibition of microsomal CYP2C11 activity by cimetidine

The effect of CIM on HO-AAVPA metabolism was evaluated in DEX-induced microsomes at different concentrations of CIM (12.5, 25, 50, 100 and 150 μM) dissolved in ethanol (0.1% final volume) and 33 μM of HO-AAVPA. The activity of the DEX-induced microsomes (CYP) in these reactions was compared with that of the control microsomes containing solvent only.

The half-maximal inhibitory concentration (IC_{50}) values were determined by linear regression analysis of the logarithm plot obtained from the per cent remaining enzymatic activity after inhibition as a function of the CIM concentration. The obtained values were converted to Ki values using the Cheng–Prusoff equation:[22] $K_i = IC_{50}/1+[S]/K_M$ at different concentrations of CIM, where K_i is the binding affinity of the inhibitor, IC_{50} is the functional strength of the inhibitor, [S] is the fixed substrate concentration, and K_M is the concentration of substrate at which the enzymatic activity is half of the maximum.

HO-AAVPA metabolic profile in rat liver microsomes

Once the reaction was quenched, microsomal incubations were processed as described in Section 2.4, and the supernatants were analysed in triplicate by injection into an ultrahigh-performance liquid chromatography instrument coupled to an electrospray ionization mass spectrometer (UPLC/ESI-MS; Waters Corporation, Milford, MA, USA). The mobile phase consisted of A) a 0.2% trifluoroacetic acid solution (v/v) at pH 3 and B) ACN 100%, in a proportion of 40% A and 60% B. The stationary phase consisted of a reversed-phase Zorbax SB-C18 column (5 μm, 4.6 × 150 mm).[20] Analysis was carried out with an isocratic flux of 0.5 ml/min. The detector used was a Bruker micrOTOF-Q II (Daltonics, Billerica, MA, USA). Analyses were performed in positive ion mode, with the nebulizer set to 5.8 psi and a scan range of 50–3000 m/z.

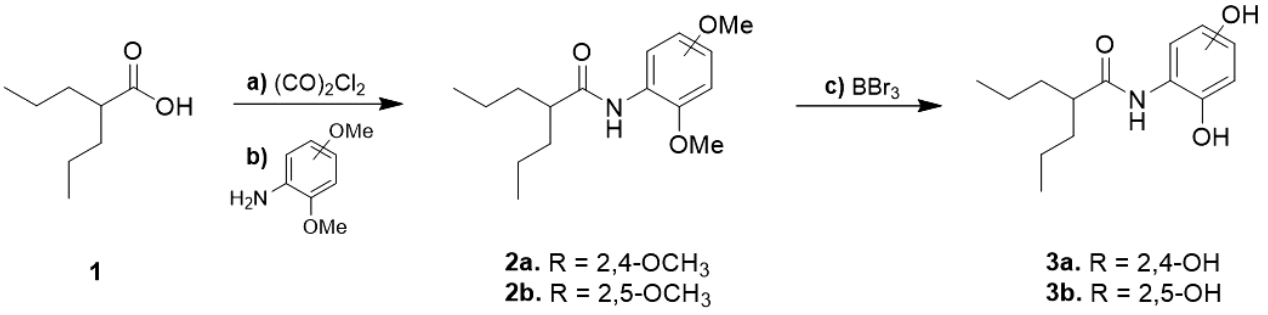

Scheme 2 Method of synthesis of the HO-AAVPA metabolites **3a** (2,4) and **3b (2,5)**. Reaction conditions: (a) 0–5°C for 1 h; room temperature for 3 h under a N_2 atmosphere. (b) DCM anh., room temperature for 12 h. (c) DCM anh., −15°C for 24 h under a N_2 atmosphere. The reaction was quenched with ice water and neutralized with $NaHCO_3$.

Substrate titrations

All experiments were carried out at room temperature in matched quartz cuvettes (1 cm × 1 cm internal) containing 2 mg/ml protein from the DEX-induced or non-induced microsomes (v/v) in 0.1 M potassium phosphate buffer, pH 7.4 with 20% glycerol.[23] Analyses were performed in a Lambda 25 UV/VIS spectrophotometer (Perkin Elmer, Waltham, MA, USA). HO-AAVPA (20 μM) was dissolved in ACN (0.2% final volume). Diclofenac and nicotine were used as substrate references, and both were dissolved in water. To obtain the spectra, a baseline was recorded with the microsomal solution added to both cuvettes (sample and reference) followed by the titration of the substrate into the sample cuvette and the titration of buffer into the reference cuvette at the same volume. Spectra were identified as type I (peak: 380–390 nm, trough: 415–420 nm) or type II (peak: 421–435 nm, trough: 390–410 nm) ligands.[24]

In silico prediction and chemical synthesis of HO-AAVPA metabolites

Before performing the synthesis (Scheme 2) of the HO-AAVPA metabolites, HO-AAVPA was submitted for the bioinformatic prediction of metabolic products by using the SMARTCyp web server (https://smartcyp.sund.ku.dk/mol_to_som). The most likely metabolites obtained from CYP metabolism proved to be 2,4-dihydroxyphenyl-2-propylpentanamide (**3a**) and 2,5-dihydroxyphenyl-2-propylpentanamide (**3b**). Once these results were determined, the chemical synthesis was carried out as described below to obtain standards of these two compounds.

General procedure for the synthesis of methoxylated intermediates (2a, 2b)

Valproic acid **1** (1.0 g, 7.50 mmol) was cooled to 0–5°C and then 1.5 eq of oxalyl chloride (0.96 ml, 11.25 mmol) was added under a nitrogen atmosphere. The mixture was stirred at 0–5°C for 1 h and then allowed to warm to room temperature for 3 h.[5] After the reaction time had elapsed, the reaction mixture was neutralized with 1 ml of a 40% trimethylamine (TEA) solution in anhydrous dichloromethane (DCM anh.). The mixture was again cooled to 0–5°C, maintaining the nitrogen atmosphere. Then, 3.0 eq of the corresponding dimethoxyaniline dissolved in DCM anh. was added slowly, and the reaction mixture was stirred for 12 h at room temperature. The course of the reaction was monitored by thin-layer chromatography (TLC) until the maximum raw material consumption was observed. Finally, the reaction was quenched by the addition of 10 ml of water, and the reaction mixture was extracted with DCM anh. (3 × 15 ml). The organic phase was washed with brine (1 × 20 ml) and dried over anhydrous sodium sulfate (Na_2SO_4 anh.). The solid was filtered under reduced pressure. The resulting crude product was purified by column chromatography using silica gel and a mixture of 95/5 hexane/ethyl acetate (EtOAc) (v/v) to give **2** as a white solid.

The chemical purity of intermediates **2a** and **2b** was analysed by HPLC with the following method: the mobile phase consisted of a mixture of A) 40% ACN and B) 60% H_2O. HPLC analysis was performed with isocratic elution and a flow rate of 0.5 ml/min. The stationary phase was a Zorbax SB-C18 column (5 μm, 4.6 × 150 mm) at a temperature of 25°C. UV detection was measured at 242 nm.

General procedure for the synthesis of dihydroxylated standards (3a, 3b)

The metabolites **3a** and **3b** were synthesized according to the general procedure in Scheme 2. Dihydroxylated derivatives were obtained by the deprotection of the methoxy groups of the respective intermediates (**2a** and **2b**).[25] Compounds **2a** and **2b** (1.0 eq) were dissolved in DCM anh. and cooled to −15°C, and then, boron tribromide (BBr_3, 10.0 eq) dissolved in DCM anh. was added dropwise

under a nitrogen atmosphere; the mixture stirred at −15°C for 24 h. Finally, to quench the reaction, the mixture was poured over ice water (50 ml) and stirred for 15 min. The aqueous layer was neutralized with a saturated solution of sodium bicarbonate ($NaHCO_3$) at pH 7 and then extracted with DCM anh. (3 × 20 ml). The organic extracts were washed with brine and dried over Na_2SO_4 anh. The solid was filtered off, and the filtrate was concentrated under reduced pressure. The products were purified by recrystallization using a mixture of DCM/hexane (5 : 1).

HPLC identification of 3a and 3b

HO-AAVPA and its previously synthesized metabolites **3a** and **3b** were analysed by the HPLC method previously reported by Silva-Trujillo *et al*.[20] to verify their retention times and for comparison to those obtained from the rat hepatic microsomes treated with HO-AAVPA.

Computational analyses

Protein model building

The amino acid sequence of the CYP2C11 rat isoform was retrieved from the Swiss-Prot entry code P08683. This sequence was submitted to BLAST analysis to identify PDB structures with the highest sequence identity. Subsequently, the structures obtained were submitted to STRAP software to confirm their sequence homology with CYP2C11. Three tridimensional (3D) structures of human CYP2C9 were available from the PDB, one apo form (PDB ID: 1OG2) and two ligand-bound complexes (PDB ID: 1OG5 and 1R9O). The crystal structure with the highest resolution (1R9O) was selected as a template for building the model of CYP2C11.

Homology modelling

A homology model of CYP2C11 was constructed using the I-TASSER hierarchical protein structure modelling approach based on the secondary structure enhanced profile–profile threading alignment (PPA) and the iterative implementation of the Threading ASSEmbly Refinement (TASSER) program. After model construction, the haem group was anchored to the catalytic site using a standard molecular docking protocol,[9] establishing molecular recognition in proximity to the atoms Fe and C^{435}.

The transmembrane segments missing from the CYP2C11 homology model were modelled as α-helices and joined to the rest of the protein by a flexible arm employing the Modeller program.[26] Then, the transmembrane helix was rotated within the membrane to be perpendicular to the membrane surface. In this CYP position, with respect to the membrane, some parts of the CYP structure in addition to the *N*-terminal membrane anchor are immersed in the POPC membrane, such as the F-G loop. These positions are in accordance with experimental reports for other CYPs.[27,28]

Ligand minimization

The 3D ligand minimum energies were achieved by means of Gaussian 09 software at the AM1 level.[29] The minimized structure was used for the docking assays.

Docking procedure

All possible rotatable bonds and partial atomic charges (Gasteiger–Marsili formalism) of the ligands, as well as the Kollman charges for all enzyme atoms of the enzyme, were assigned using the AutoDock tool 1.5.4.[30] Afterward, the ligands were docked into CYP2C11 using AutoDock 4.2.0 with the hybrid Lamarckian genetic algorithm as the search method, with an initial population of 100 randomly placed individuals and a maximum energy of evaluation of 1.0×10^7. All docking simulations were performed using a grid box on all proteins (120 $Å^3$) centred on the haem group with grid points separated by 0.375 $Å^3$. All protein visualizations were performed with PyMOL DeLano WL (http://www.pymol.org).

Molecular dynamics (MD) simulations

Anchoring the complexes into a POPC membrane

The CYP2C11/HO-AAVPA complexes were oriented with respect to the lipid membrane using the OPM (Orientations of Proteins in Membranes) server (http://opm.phar.umich.edu/). A rectangular pre-equilibrated POPC phospholipid bilayer was generated for each system using the membrane-builder tool of CHARMM-GUI[31] (111.416 × 111.416 × 125.962 Å, XYZ). To place the CYP2C11/HO-AAVPA complex into the bilayer, the replacement method was used.[32,33] The membrane consisted of 338 POPC phospholipids with 161 on the top and 177 on the bottom. The size along the *z*-axis (125.962 Å) was determined by specifying the thickness of bulk water from the protein extent along Z (Z centre = 24.356). The membrane–receptor complexes obtained were thus solvated and neutralized using the solvation and autoionized modules (ion placing method) of the charm-gui membrane builder.[31] The ionic strength was maintained at 0.15 M NaCl using the TIP3 water model. The all-atom models of each system were generated by using the CHARMM force-field parameters (http://mackerell.umaryland.edu/CHARMM_ff_params.html). Then, these files were

converted into files that conformed to the Lipid11 naming convention using the charmmlipid2amber.x script included in the AMBER 12 package.[34] Lipid11 is the Amber lipid force field that includes parameters from the general Amber force field (GAFF).[35,36] Starting from the CYP2C11/ligand complex obtained through docking procedures, the topologies to perform MD simulations were constructed using the Leap module with the ff99SB and Lipid11 force fields.[37,38] The ligand topologies were built with the antechamber module, based on the generalized AMBER force field (GAFF)[36] followed by *ab initio* optimization at the AM1-BCC level.[37] The missing force-field parameters for the haem (all-atom) group were taken from the AMBER parameter database at http://www.pharmacy.manchester.ac.uk/bryce/amber (Accessed March 13, 2013). Then, these structures were minimized and heated with sander following three steps. First, the systems were submitted for energy minimization during 10 000 steps under the NVT ensemble, with position restraints (the force constant was set to 500 kcal mol^{-1} $Å^{-2}$) on both the protein and lipids to allow for the relaxation of the water molecules. After this equilibration step, the system was slowly heated in the NPT ensemble through two sequential runs from 0 to 300 K while keeping the protein atoms and lipids restrained (the force constant was set to 10 kcal mol^{-1} $Å^{-2}$). First, the system was heated from 0 to 100 K using the Langevin thermostat, and the second phase of heating consisted of slowly increasing the temperature to the production temperature (300 K). The positions and velocities were read from the previous temperature heating, and an anisotropic Berendsen weak-coupling barostat[38] was used to equilibrate the pressure, whereas the Langevin thermostat was used to equilibrate the temperature.

The MD simulations were performed with pmemd.cuda AMBER 12 executable,[34] which allowed the acceleration of explicit solvent particle mesh Ewald (PME) calculations[39] through the use of GPUs.[40,41] MD simulations of 150 ns in length were run with the input files without position restraints under periodic boundary conditions (PBC) and using an NPT ensemble at 300 K. The electrostatic interactions were calculated via the particle mesh Ewald method,[39] and a 10 Å cut-off was used for the van der Waals interactions. The bonds between the heavy atoms and hydrogens were constrained with the SHAKE algorithm.[42] The temperature was controlled using Langevin dynamics while the pressure was controlled using a semi-isotropic constant surface tension to maintain a specific area per lipid. The collision frequency was 1.0 ps^{-1}. The pressure was maintained at 1 bar, and the pressure coupling constant was set to 1 ps. The time step of the MD simulations was set to 2.0 fs, and the coordinates were saved for analysis every 1 ps.

Analysis of MD trajectories

The ptraj module of Amber 12 was used to analyse the root-mean-square deviation (RMSD) between structure pairs. The area per lipid was calculated using the cpptraj module of Amber 12 by dividing the area of our simulation box [(box X length) × (box Y length)/(number of phospholipids per layer)]. Before the RMSD calculations, the overall translational and rotational motions were removed, and the RMSD was calculated for all heavy atoms. Average conformations were obtained through a cluster analysis using the kclust algorithm that belongs to the MMTSB toolset (http://mmtsb.scripps.edu/software/mmtsbtoolset.html). Then, from the most populated cluster, the conformation with the lowest RMSD to the cluster centre (centroid) was selected. Images were prepared using PyMOL v0.99.

Calculation of absolute binding free energies

Calculations of the absolute binding free energies were performed using the MMGBSA method[43–45] following the single-trajectory approach. By using this methodology, the molecular structures of the binding partners are taken from the CYP2C11/HO-AAVPA complexes generated during the MD simulation. Although the energetic contributions due to the conformational changes are ignored, this approach leads to a strong decrease in the statistical uncertainty of the free energy components.[43]

Before the calculations were performed, all counter ions and water molecules were stripped from the snapshots for each system, and 800 snapshots at time intervals of 100 ps from the last 80 ns of the simulations runs were taken, using a salt concentration of 0.1 M and the Born implicit solvent model of 2 (igb = 2). The analyses were performed using the MMPBSA perl script[44] provided in the Amber 12 package.[34] The binding free energy (ΔG_{bind}) of each complex can be calculated as $\Delta G_{bind} = G^{complex} - G^{receptor} - G^{ligand} = \Delta E_{MM} + \Delta G_{GB} + \Delta G_{SA} - T\Delta S$, where ΔE_{MM} is the gas-phase interaction energy between the receptor and the ligand, which includes the van der Waals (ΔE_{vdw}) and the electrostatic (ΔE_{ele}) interaction energies. ΔG_{GB} and ΔG_{SA}, respectively, are the electrostatic and non-polar contributions to desolvation upon ligand binding, and $-T\Delta S$ is the entropy contribution resulting from the change in the degrees of freedom of the solute molecules, which were considered here; therefore, our values reported for the MMGBSA calculations should be named absolute binding free energies.

Entropic contributions were evaluated using the MMPBSA.py module implemented in Amber Tools 1.5,[34] and only 40 snapshots taken at time intervals of 2 ns were chosen due to the large memory demand for this calculation.

Statistical analysis

HO-AAVPA consumption rate and M1 formation data were processed using the non-linear regression method, and the effect of different concentrations on consumption rate was analysed by the one-way ANOVA method and the post hoc Tukey's multiple comparison test. Data of inhibition of HO-AAVPA metabolism and the formation of M1 and M2 by CIM were analysed by the two-way ANOVA test method. The interaction of HO-AAVPA with rat hepatic non-induced and DEX-induced microsomes, measured as the CYP optical difference spectra, was analysed by paired Student's *t*-test. In all cases, a value of $P < 0.05$ was considered to establish a statistically significant difference. All analyses and the corresponding graphs were performed in GraphPad 5.01.

Results

Metabolic activity of microsomal CYP enzymes on HO-AAVPA

Figure 1 shows the chromatograms of HO-AAVPA[20] as well as those corresponding to the incubation of HO-AAVPA in the presence of either non-induced (Figure 1b) or DEX-induced microsomes (Figure 1d). For the DEX-induced microsome incubations, only one signal appeared at 5.3 min, in addition to the respective controls (Figure 1a and 1c). These findings demonstrate that pretreatment of rats with DEX resulted in a 1.7-fold enhancement in HO-AAVPA metabolic activity in the liver. CYP activity was determined by quantification of the HO-AAVPA consumption (Figure 2a) and M1 production (Figure 2b). Screening for metabolic activity from 5 to 250 μM HO-AAVPA allowed for determination of the K_M and V_{max} values, which were 26.43 ± 1.75 μM and 0.126 ± 0.006 μM/min/nmol CYP, respectively (Table 1).

Effect of CIM inhibition on CYP-mediated metabolism of HO-AAVPA

The presence of CIM in the rat liver microsomes incubations decreased the consumption of HO-AAVPA through CYP2C11 inhibition. As shown in Figure 2c, when the maximum concentration of CIM (150 μM) was used, the consumption of HO-AAVPA was inhibited in rat liver microsomes by 67.05% ± 24.87% ($P > 0.05$), while the production of M1 and M2 decreased by 52.07% ± 9.89%

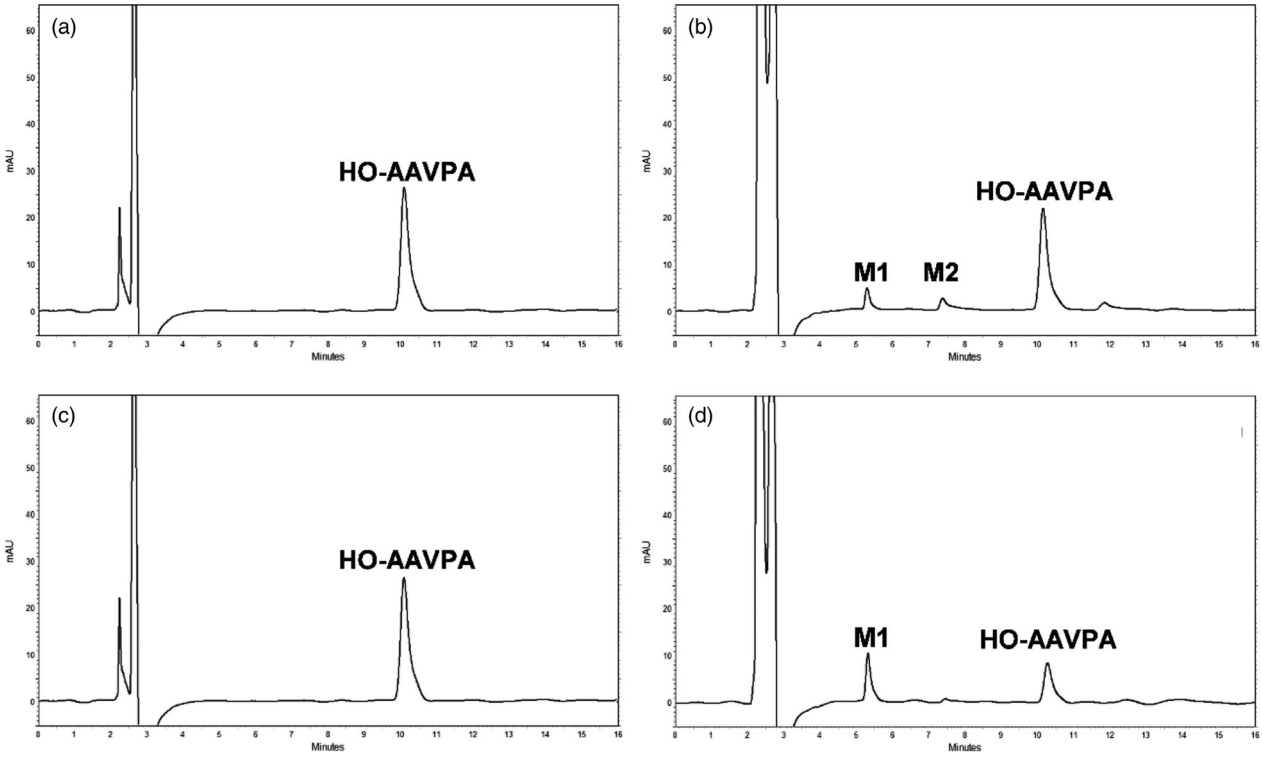

Figure 1 Representative UV-HPLC chromatograms of the HO-AAVPA metabolism by rat liver microsomes. (a) Control in the absence of NADPH in non-induced microsomes. (b) Full reaction in non-induced microsomes. (c) Control in the absence of NADPH in DEX-induced microsomes. (d) Full reaction in DEX-induced microsomes.

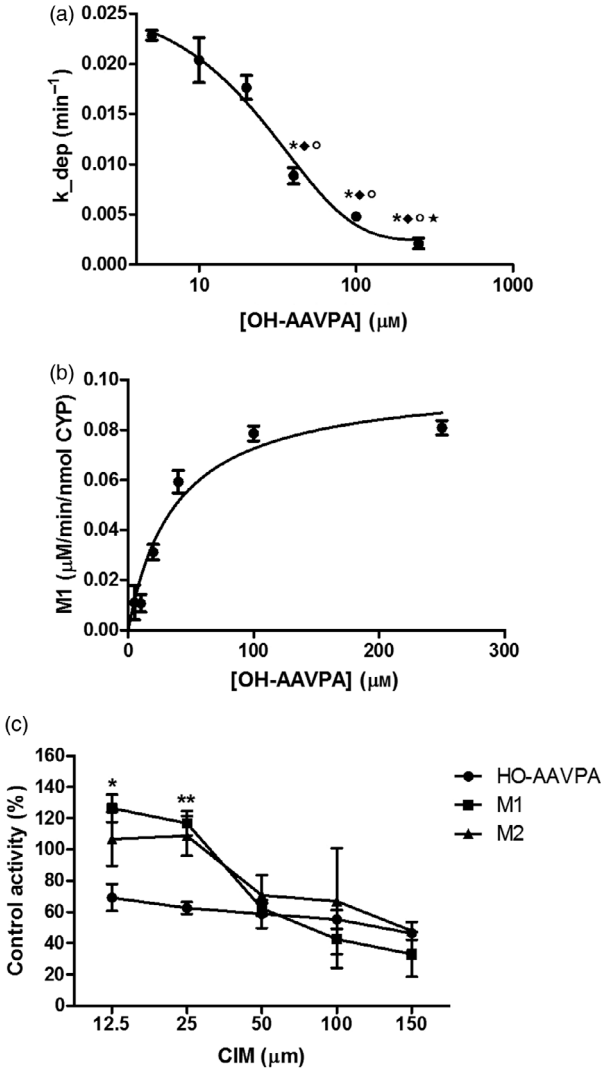

Figure 2 (a) Depletion curve of HO-AAVPA in the range of 5–250 μM in DEX-induced microsomes and 30 min of incubation time. Each point represents the mean of three independent replicates ($n = 3$). $P < 0.05$: *[5] vs [40], [100] and [250]; ♦[10] vs [40], [100] and [250]; °[20] vs [40], [100] and [250]; [40] vs [250]. (b) Michaelis–Menten plot for M1 production. Reactions were performed with 5–250 μM HO-AAVPA in the presence of 0.3 mg/ml DEX-induced microsomes and 30 min of incubation time. Each point is the mean of three independent replicates ($n = 3$). (c) Plot of the inhibition of HO-AAVPA consumption and formation of M1 and M2 by increasing the concentration of CIM. Results are given as the mean values of five independent replicates ($n = 5$). $P = 0.0365$ (among groups) and $P < 0.0001$ (among concentrations): *12.5 μM (HO-AAVPA vs M1 and M2); **25 μM (HO-AAVPA vs M1 and M2).

and 53.68% ± 4.95% ($P > 0.05$), respectively. These results revealed that CIM was able to decrease the formation of M1 and M2, suggesting involvement from CYP2C11 in the biotransformation of HO-AAVPA to yield these metabolites.

Table 1 K_M, V_{max} and CL_{int} values determined using product formation measurements and substrate depletion measurements for rat hepatic microsomes induced with DEX

Parameter	Substrate depletion (Mean ± SD)	Product formation (Mean ± SD)
K_M (μM)	26.43 ± 1.75	38.94 ± 1.69
V_{max} (μM/min/nmol CYP)	0.126 ± 0.006	0.0976 ± 0.003
CL_{int} (μl/min/mg protein)	108.53 ± 12.55	59.05 ± 1.00

Metabolic profile study in rat liver microsomes

The chromatogram of non-induced microsomes incubated with HO-AAVPA (Figure 1b) showed the same retention time for HO-AAVPA at 10.1 min (Figure 3a). In addition, two new peaks at 5.3 and 7.4 min were detected, suggesting the presence of two metabolites (M1 and M2, respectively) (Figure 1b and 1d). However, due to the low quantity of M2, only metabolite M1 was further analysed by MS (Figure 4). For M1, one peak at 252.2 m/z was detected, which corresponds to the hydroxylation of HO-AAVPA (236.2 m/z; Figure 4). To support our hypothesis that M1 could be a product of HO-AAVPA hydroxylation as predicted with the SMARTCyp platform (Figure 5), we synthesized the corresponding standards **3a** and **3b** as described in Section 2.8 to be further characterized (Figures S1–S5). These compounds, **3a** and **3b**, show approximately the same HPLC retention time (≅5.4 min, Figure 3), and the MS molecular ions correspond to 252.1595 and 252.1596 m/z, respectively (Figures 4 and S5).

Substrate titrations

The UV spectra were used to determine the absorbance differential (ΔA) exhibited by HO-AAVPA consumption, as well as its binding mode with CYP enzymes present in rat liver microsomes. In Table 2, it can be observed that the ΔA value is higher in DEX-induced microsomes than that in the non-induced microsomes. Furthermore, the peak values (Figure 6 and Table 2) show that HO-AAVPA exhibits a type I ligand binding mode with the microsomal CYP enzymes.

Chemical synthesis of standards 3a and 3b

Intermediate 2,4-dimethoxyaniline-2-propylpentanamide (2a)

For **2a** preparation, the general procedure was followed using 2,4-dimethoxyaniline (2.8 g, 18.46 mmol) dissolved

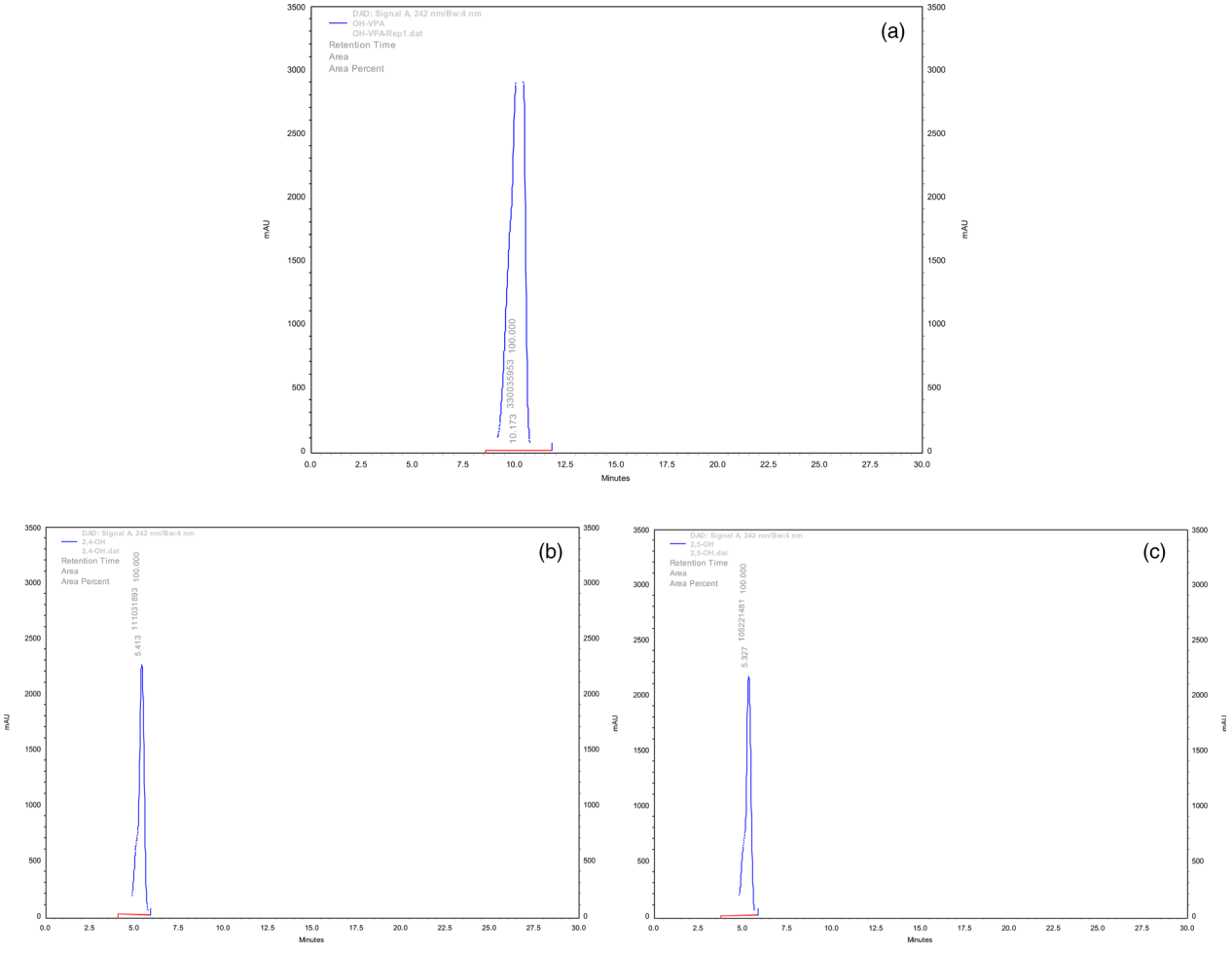

Figure 3 Liquid chromatograms of (a) HO-AAVPA, (b) metabolite **3a** and (c) metabolite **3b**.

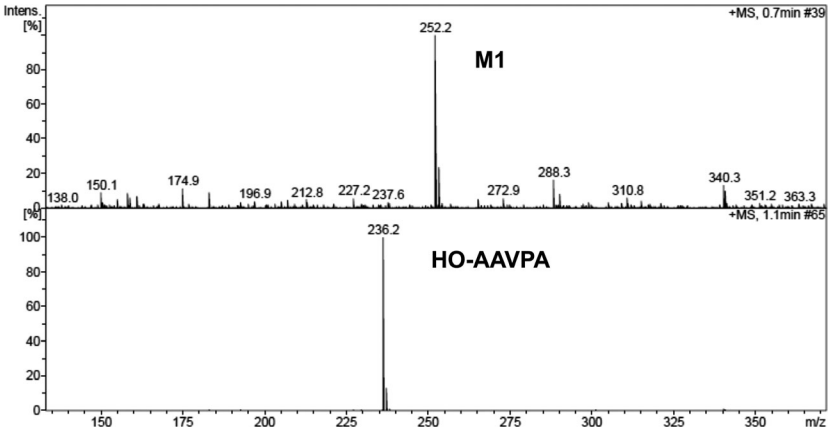

Figure 4 HO-AAVPA submitted for LC-MS study after metabolism in rat liver microsomes.

in 14.0 ml of DCM anh. After purification by column chromatography, the solid obtained was recrystallized from a DCM/hexane mixture (1 : 5), obtaining 2,4-dimethoxyaniline-2-propylpentanamide (**2a**) as white crystals (0.89 g, 48.0% yield), with a R_f of 0.46 (hexane/EtOAc, 8 : 2) and a melting point of 106–107°C. FTIR (ATR)

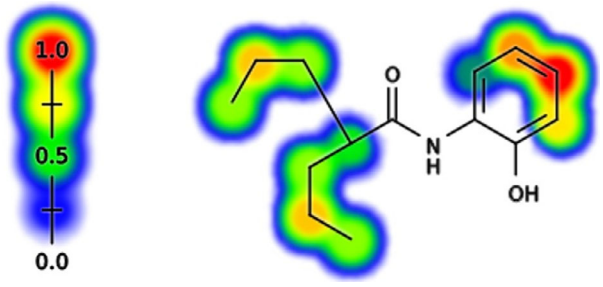

Figure 5 Predicted HO-AAVPA sites for metabolism of by the CYP2C9 isoform using SmartCyp. Red colour (1) means high possibility to be chemically modified from CYPs. Orange colour means 50% to be chemically modified from CYPs. Blue colour means lowest possibility (0) to be chemically modified from CYPs.

νmax: 3289, 2929, 1655, 1533, 1452, 1412, 1281, 1211, 1159, 1123, 1035, 825, 685 cm^{-1}. ^1H NMR (750 MHz, DMSO-d_6) δ: 8.86 (s, 1H, NH), 7.57 (d, J = 8.25 Hz, 1H, H-6), 6.60 (d, J = 2.25 Hz, 1H, H-3), 6.47 (dd, J = 6.75, 2.25 Hz, 1H, H-5), 3.79 (s, 3H, OMe), 3.74 (s, 3H, OMe), 2.51-2.47 (m, 1H, H-8), 1.55-1.49 (m, 4H, H-9, H-9′), 1.33-1.26 (m, 4H, H-10, H-10′) 0.88 (*t*, J = 6.75 Hz, 6H, H-11, H11′) (Figure S1A). ^{13}C NMR (188.5 MHz, DMSO-d_6) δ: 174.58 (C-7), 157.45 (C-4), 152.56 (C-2), 125.16 (C-6), 120.77 (C-1), 104.43 (C-5), 99.27 (C-3), 56.15 (OMe), 55.73 (OMe), 45.85 (C-8), 35.50 (C-9, C-9′), 20.62 (C-10, C10′), 14.53 (C-11, C-11′) (Figure S1B). ESI-MS for $C_{16}H_{25}NO_3$. Calculated [M + H]: 279.18. Found [M + H]+: 280.1930 (Figure S5A). HPLC purity: 99.6%. Retention time: 5.4 min.

Intermediate 2,5-dimethoxyaniline-2-propylpentanamide (2b)

For **2b** preparation, the general procedure was followed using 2,5-dimethoxyaniline (2.8 g, 18.46 mmol) dissolved in 14.0 ml of DCM anh. After purification by column chromatography, the solid obtained was recrystallized from a DCM/hexane mixture (5 : 1), obtaining 2,5-dimethoxyaniline-2-propylpentanamide as white crystals (0.91 g, 49.0% yield), with a R_f of 0.53 (hexane/EtOAc, 8 : 2) and a melting point of 70–71°C. FTIR (ATR) νmax: 3259, 2952, 1652, 1591, 1458, 1427, 1278, 1212, 1123, 1054, 866, 787, 718 cm^{-1}. ^1H NMR (750 MHz, DMSO-d_6) δ: 8.95 (s, 1H, NH), 7.67 (d, J = 3.75 Hz, 1H, H-6), 6.93 (d, J = 9.00 Hz, 1H, H-3), 6.62 (dd, J = 9.00, 3.00 Hz, 1H, H-4), 3.76 (s, 3H, OMe), 3.67 (s, 3H, OMe), 2.61-2.58 (m, 1H, H-8), 1.53-1.48 (m, 4H, H-9, H-9′), 1.33-1.23 (m, 4H, H-10, H-10′) 0.86 (*t*, J = 7.50 Hz, 6H, H-11, H11′) (Figure S2A). ^{13}C NMR (188.5 MHz, DMSO-d_6) δ: 175.00 (C-7), 153.37 (C-5), 144.22 (C-2), 128.67 (C-1), 112.40 (C-6, 109.01 (C-4), 108.55 (C-3), 56.76 (OMe), 55.79 (OMe), 46.08 (C-8), 35.44 (C-9, C-9′), 20.61 (C-10, C10′), 14.52 (C-11, C-11′) (Figure S2B). ESI-MS for $C_{16}H_{25}NO_3$. Calculated [M + H]: 279.18. Found [M + H]+: 280.1909 (Figure S5B). HPLC purity: 98.4%. Retention time: 4.4 min.

Table 2 Rat hepatic microsomal CYP optical difference spectra in the presence of HO-AAVPA (n = 5)

Microsomes	Δ*A* (Mean ± SD)	Wavelength (nm, Mean ± SD)	
		Trough	Peak
Without treatment	0.0022 ± 0.0007	418 ± 3.9	392 ± 1.7
DEX-induced	0.0040 ± 0.0019	418 ± 3.8	392 ± 8.5

Metabolite 2,4-dihydroxyphenyl-2-propylpentanamide (3a)

To a solution of **2a** (0.5 g, 3.25 mmol) in DCM anh. (5.0 ml), BBr3 (1.7 ml, 17 mmol) dissolved in anh. DMC (2.0 ml). After recrystallization, **3a** was obtained as white crystals (0.201 g, 25% yield), with a R_f of 0.45 [5% TEA-hexane, DCM/methanol (MeOH), 1 : 1] and a melting point of 89-90 °C. FTIR (ATR) νmax: 3361, 3247, 2928, 2870, 1598, 1510, 1164, 1108, 975, 795 cm^{-1}. ^1H NMR (750 MHz, DMSO-d_6) δ: 9.30 (s, 1H, OH-2), 8.92 (s, 1H, NH), 8.78 (s, 1H, OH-4), 7.12 (d, J = 2.9 Hz, 1H, H-6), 6.66 (d, J = 8.6 Hz, 1H, H-5), 6.39 (dd, J = 8.6, 2.9 Hz, 1H, H-3), 2.56 (dd, J = 9.6, 4.8 Hz, 1H, H-8), 1.53 (tt, J = 13.2, 9.4, 5.6 Hz, 4H, H-9, H-9′), 1.38–1.21 (m, 4H, H-10,H-10′), 0.88 (*t*, J = 7.4 Hz, 6H, H-11, H-11′) (Figure S3A). ^{13}C NMR (188.5 MHz, DMSO-d_6) δ: 175.516 (C-7), 155.85 (C-4), 150.47 (C-2), 124.71 (C-1), 118.50 (C-5), 106.50 (C-6), 104.19 (C-3), 45.80 (C-8), 35.44 (C-9, C-9′), 20.66 (C-10, C-10′), 14.48 (C-11, C-11′) (Figure S3B). ESI-MS for $C_{14}H_{21}NO_3$. Calculated [M + H]: 251.3260. Found [M + H]+: 252.1595 (Figure S5C). HPLC purity: 99.0%. Retention time: 5.4 min.

Metabolite 2,5-dihydroxyphenyl-2-propylpentanamide (3b)

To a solution of **2b** (0.5 g, 3.25 mmol) in DCM anh. (5 ml), BBr3 (1.7 ml, 17 mmol) dissolved in anh. DMC (2 ml). After recrystallization, **3b** was obtained as white crystals (0.315 g, 39% yield), with a R_f of 0.51 (5% TEA/hexane, DCM/MeOH, 1 : 1) and a melting point of 109–111°C. FT IR (ATR) νmax: 3285, 3126, 2962, 2875, 1647, 1539, 1450, 1187, 971, 872, 736 cm^{-1}. ^1H NMR (750 MHz, DMSO-d6) δ: 9.29 (s, 1H, OH-2), 8.90 (s, 1H, NH), 8.76 (s, 1H, OH-5), 7.11 (d, J = 3.0 Hz, 1H, H-6), 6.65 (d, J = 8.7 Hz, 1H, H-3), 6.38 (dd, J = 8.5, 3.0 Hz, 1H, H-4), 2.55 (dd, J = 9.6, 4.9 Hz, 1H, H-8), 1.56–1.48 (m, 4H,

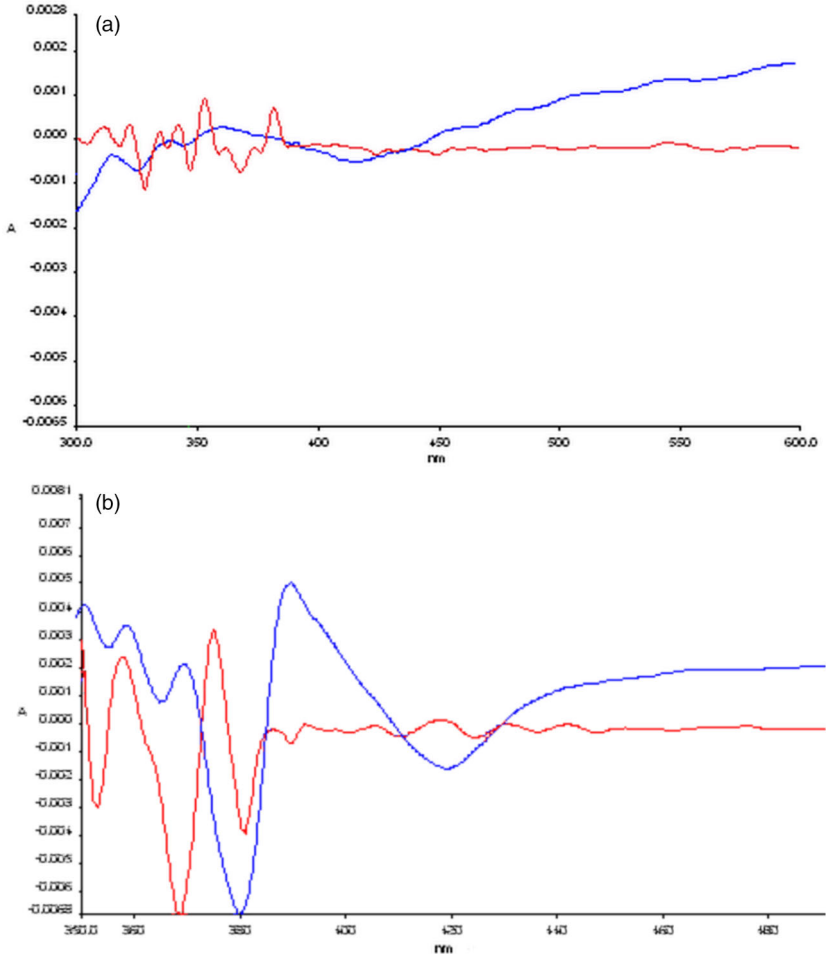

Figure 6 Absolute spectra of rat microsomal CYP in 20% glycerol, 100 mM sodium phosphate, pH 7.4 and HO-AAVPA (20 μM) at room temperature. Red lines show the basal line, and blue lines show the spectrum after HO-AAVPA addition in (a) untreated microsomes and (b) DEX-induced microsomes.

H-10), 1.33 (tt, J = 12.8, 10.3, 5.5 Hz, 4H, H-9), 1.31–1.21 (m, 4H, H-10), 0.92–0.84 (m, 6H, H-11) (Figure S4A). ^{13}C NMR (188.5 MHz, DMSO) δ: 175.44 (C-7), 150.31 (C-5), 140.88 (C-2), 127.10 (C1), 117.33 (C-3), 111.83 (C-4), 109.62 (C-6), 46.09 (C-8), 35.44 (C-9, C-9′), 20.64 (C-10, C-10′), 14.46 (C-11, C-11′) (Figure S4B). ESI-MS for $C_{14}H_{21}NO_3$. Calculated [M + H]: 251.3260. Found [M + H]+: 252.1596 (Figure S5D). HPLC purity: 99.0%. Retention time: 5.3 min.

Molecular docking

CYP2C9 exhibits high regioselectivity and catalytic efficiency for the oxidation of diclofenac.[46] Since CYP2C11 and CYP2C9 share high-sequence identity (77%), it could be expected that HO-AAVPA binds to CYP2C11. Figure 7a depicts that HO-AAVPA reached the substrate binding site, which is formed by the following secondary structure elements: helices I, F, and G; loop F-G; and loop B-C. HO-AAVPA bound to the CYP2C11 substrate binding site adopted a conformation in which most of the contacts (residues within a distance of 4 Å) are predominantly hydrophobic (Figure 7b), as has been observed in some modelling and crystallographic CYP complexes.[9,47] In this ligand conformation, the hydroxyphenyl ring of HO-AAVPA (C-3 atom) is placed in close proximity to the haem group and iron atom (Fe) (Figure 7b), with an average distance of approximately 4.7 Å and an angle of 37.2°, whereas C-4 is located 6.05 Å from the haem iron atom. These atomic distances are in agreement with the hydroxylation of steroid molecules[48] and VPA.[9] The calculated docking energy was −6.77 kcal/mol, and the theoretical K_d was 10.9 μM. This binding pose suggests that the active high-valent iron-oxo could attack both C-3 and C-4 during the oxidation reaction since these two carbons are close to the oxo atom.

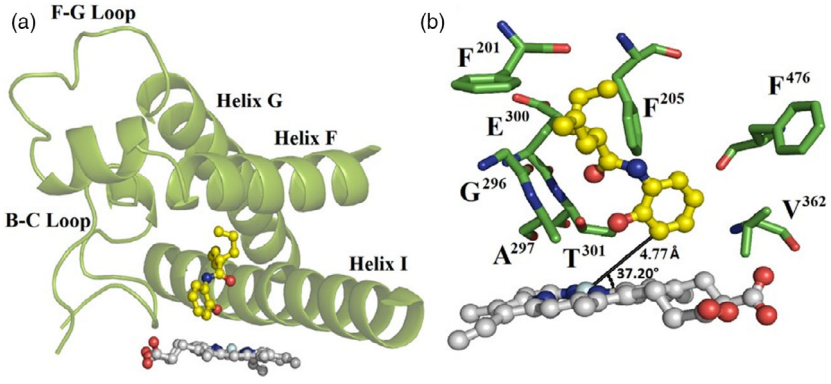

Figure 7 (a) Secondary structure elements forming the substrate binding site of the CYP2C11-HO-AAVPA complex. (b) Residues at a distance ≤4 Å stabilizing the CYP2C11-HO-AAVPA complex predicted through docking calculations. The protein is shown as the green cartoon representation, the ligand is shown as the yellow ball-and-stick representation, the haem group is represented as the white ball-and-stick representation, and the residues that stabilize the complex are shown as the green stick representation.

MD simulations

Convergence and equilibrium examination

To verify the robustness and stability of the CYP2C11/HO-AAVPA complex, long MD simulations were performed for complexes anchored into a POPC membrane (Figure 8a) considering the physiological environment for this system.[49,50] To evaluate whether the systems reached the equilibrium stages, some structural properties during the MD simulation were monitored, such as the root-mean-square deviation (RMSD) of the backbone atoms with respect to the initial structure and the area per lipid. Figure 8b shows that the CYP2C11/HO-AAVPA complex exhibits a very high area per lipid value at the beginning of the simulation and then decreases towards a converged area per lipid on the order of 60–70 ns, obtaining an area per lipid value of 56.57 ± 0.70 for CYP2C11/HO-AAVPA. These findings are in good agreement with those found for other protein-POPC-membrane systems.[50,51] Similarly, RMSD analysis shows that the CYP2C11/HO-AAVPA complex reached convergence on the order of 60-70 ns (Figure 8c). Therefore, all structural analyses and free energy calculations were performed on the last 80 ns of the 150 ns of the MD simulations.

Interactional analysis and average properties

The detailed map of interactions was explored under physiological environmental conditions generated through MD simulations that incorporate water molecules, protein flexibility, and a membrane environment. The most populated conformations for the two complexes were calculated through a cluster analysis for the last 80 ns of the MD simulations (see methods). The MD simulations showed that the ligand conformation predicted by the docking procedures was conserved with some small conformational differences. For the CYP2C11-HO-AAVPA complex, the cluster analysis yielded three complex conformations, representing 31.60, 23.70 and 15.6% of the entire present conformations, corresponding to the first, second and third most populated conformations, respectively. Figure 9 shows the three most populated complex conformations present during the last 80 ns of the MD simulation for CYP2C11/HO-AAVPA. Figure 9a shows that the ligand conformations are roughly similar for the three HO-AAVPA conformations, with RMSD values that oscillate between 0.28 and 1.6 Å. However, some differences can be observed when a more detailed analysis is performed. Figure 9b shows the residues at a distance of 4 Å stabilizing the first most populated ligand conformation, where the ligand is stabilized through hydrophobic contacts, with either the side chain or backbone atoms of V^{102}, I^{113}, N^{204}, F^{201}, F^{205}, F^{208}, E^{300}, T^{301}, L^{361} and L^{366}, positioning the C-3 atom of the hydroxyphenyl ring of HO-AAVPA in close proximity to the iron (Fe) atom of the haem group, with an average distance of approximately 4.54 Å, whereas C-4 is located 5.27 Å from the Fe atom of the haem. These atomic distances are in agreement with the hydroxylation of steroid molecules and are similar to those generated by the docking procedures.[10] The second most populated conformation was stabilized by similar hydrophobic residues as those observed for the first conformation (Figure 9c). However, some interactions with other residues were present that were not observed for the first conformation (F^{114} and V^{362}). In this ligand conformation, the hydroxyphenyl ring was also close to the haem group with the C-5 atom in the closest proximity to the Fe atom, with an average distance of approximately 4.28 Å, whereas C-4 was located 5.27 Å from the Fe atom of the haem, an identical value to that observed for the first most populated conformation. The third most populated conformation also shared a similar map of

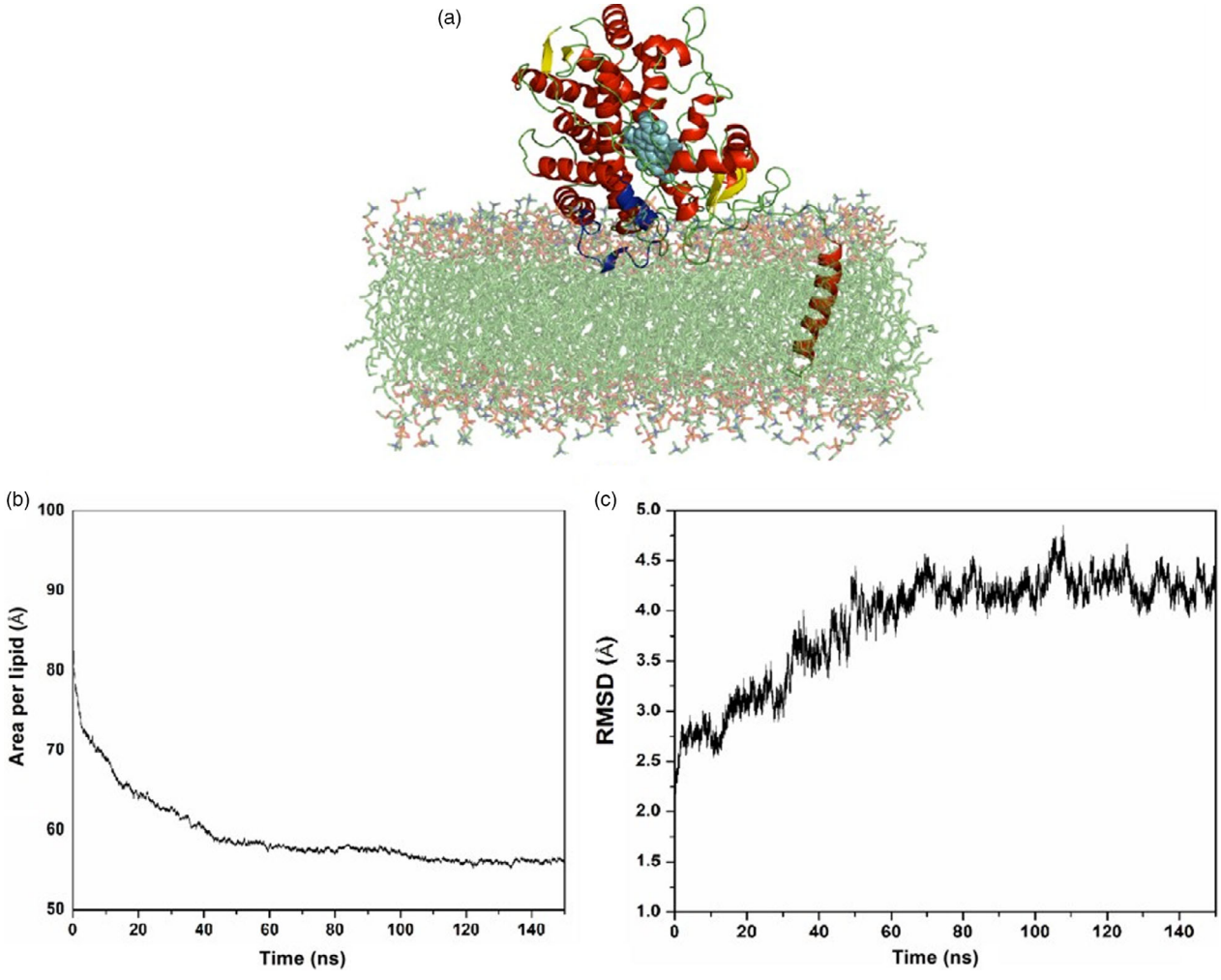

Figure 8 MD simulation box and equilibrium properties of the CYP2C11-HO-AAVPA complex. (a) MD simulation box of the extracellular and transmembrane regions of the CYP2C11-HO-AAVPA complex embedded in the POPC membrane. (b) Area per lipid. (c) RMSD analysis. Secondary structure elements of CYP2C11 are depicted in red (α-helix), yellow (β-sheets) and green (loops). The last conformation from the 150 ns long MD simulation of the CYP2C11-HO-AAVPA complex was selected for representation.

interactions as the first and second ligand conformations, adding a new hydrophobic contact with F^{237}, whereas the C-3 atom showed a similar distance to the first conformation, with an average value of 4.38 Å from the haem Fe atom (Figure 9d). Overall, these results suggest that HO-AAVPA reaches a conformation that is quite stable in the substrate binding site of CYP2C11, maintaining a similar map of interactions as those predicted through the docking procedures. Moreover, to obtain a more refined simulation of the protein–ligand interactions than the one obtained from docking methods, MD simulations were performed. A clear example of this was noticed between several phenylalanine cluster elements and HO-AAVPA, for which the more energetically stabilized $\pi - \pi$ interactions were observed from the MD simulation results (Figure 9b–d).

Free energy calculations

To obtain the energetic contribution of the HO-AAVPA-CYP2C11 complex, the electrostatic energies, non-polar solvation, van der Waals interactions and total contribution from the binding free energy values were calculated using the MMGBSA method (see Materials and Methods). Our analysis shows that the ligand–protein complex formation is mainly driven by non-polar interactions ($\Delta E_{vwd} + \Delta G_{npol,sol}$), with the ΔE_{vwd} interactions making the major contribution and the polar ($\Delta E_{ele} + \Delta G_{ele,sol}$) interactions being unfavourable to the molecular recognition (Table 3). These energetic contributions agree with the map of interactions observed for the most populated conformations between CYP2C11 and HO-AAVPA, for which all the complexes are mainly stabilized

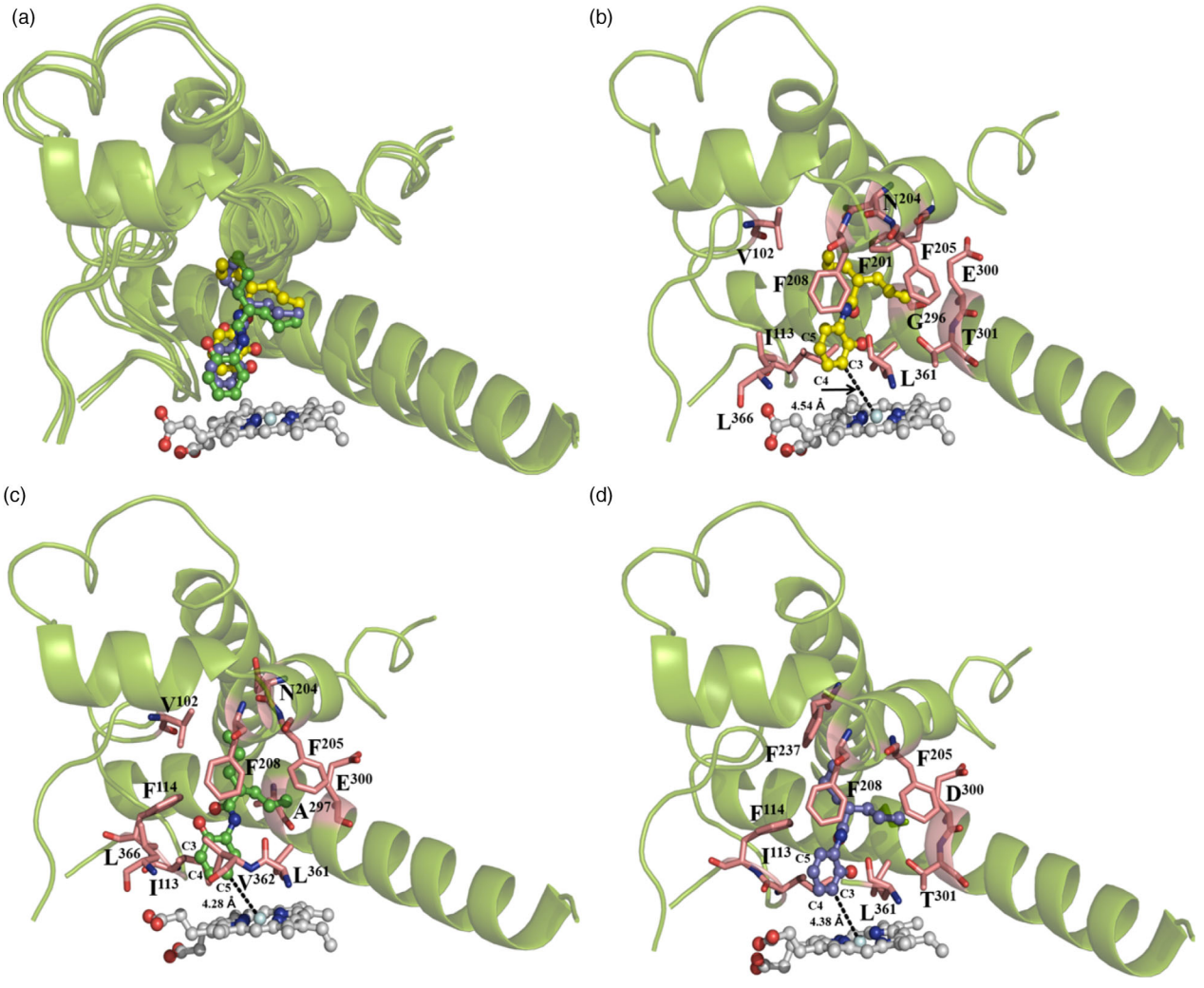

Figure 9 The three most populated conformations of HO-AAVPA into the active site of CYP2C11. (a) Structural superposition of the three most populated conformations of CYP2C11-HO-AAVPA. (b) The first most populated conformation. (c) The second most populated conformation. (d) The third most populated conformation. Residues at a distance of ≤4 Å stabilizing the CYP2C11-HO-AAVPA complex are shown in the salmon stick representation.

Table 3 Binding free energy components of the CYP–ligand complexes (in units of kcal/mol)

System	ΔE_{vdw}	ΔE_{ele}	$\Delta G_{ele,sol}$	$\Delta G_{npol,sol}$	ΔE_{polar}	ΔE_{npol}	ΔG_{mmgbsa}	$-T\Delta S$	ΔG_{bind}
CYP2C11-HO-AAVPA	−38.70 (0.16)	1.22 (0.11)	11.87 (0.11)	−4.78 (0.02)	13.90	−43.48	−29.58 (5.6)	−14.05 (2.65)	−15.53

Polar (ΔE_{ele} + $\Delta G_{ele,sol}$) contributions (ΔE_{polar}) and non-polar (ΔE_{vwd} + $\Delta G_{npol,sol}$) contributions (ΔE_{npol}). All the energies were averaged over several snapshots (see Methods) and are given in kcal/mol (±standard error of the mean).

through hydrophobic interactions (Figure 9b–d). The entropic component indicates a decrease in the conformational mobility upon the formation of the complex, which is the product of a reduction in the number of degrees of freedom, contributing to an unfavourable entropy component in the calculated binding free energy, bringing this calculated value close to the experimental values. Overall, these ΔG_{bind} values for HO-AAVPA are more energetically favourable than those observed for VPA.[9]

Discussion

Reducing the toxic effects of a widely used therapeutic drug is one of the main objectives in drug development. VPA has been reported to be a hepatotoxic drug, and this effect is attributed to its CYP-dependent metabolism.[3,4] This effect represents a high risk when VPA is administered continuously for long periods of time.[52,53] For this reason, the aryl VPA derivative HO-AAVPA has been proposed as a

potential anticancer agent based on previous studies.[5] Hence, to contribute to the HO-AAVPA metabolic assessment, we performed *in vitro* (Figures 1–4 and 6) and *in silico* (Figures 7–9) studies to evaluate the CYP-mediated metabolism of HO-AAVPA.

The *in vitro* assays were developed with rat liver microsomes to determine the HO-AAVPA metabolism and revealed a metabolite named M1 (Figure 1). Thus, experimental assays show typical saturation kinetics, showing concentration-dependent activity (Figure 2). Furthermore, with the obtained kinetic parameters, it was possible to demonstrate that the metabolic activity in DEX-induced microsomes was higher than that in the untreated microsomes (Figures 1 and 2), proving that DEX is a potent inducer of CYP enzymes.[12] Previous studies have shown that DEX levels play an important role in the upregulation of CYP2C11 expression and, consequently, in its participation in microsomal oxidation reactions. Specifically, this effect has been observed *in vitro* where activation of CYP2C11 was detected when low concentrations of DEX were added to rat hepatocyte cultures[12,54] Likewise, this effect has been observed *in vivo* using Sprague-Dawley rats treated with DEX.[55] Despite the fact that the kinetic parameters obtained in our study could not be attributed to the activity of a specific isoform, the obtained results from the induction of rat liver microsomes with DEX and their inhibition with CIM suggest that CYP2C11 is a main isoform that participates in the HO-AAVPA biotransformation.[13,14]

For *in vitro* studies, the results presented here suggest that the K_M and V_{max} values obtained from the substrate depletion method can be used to make inferences about the metabolism of a compound (Table 1). This method is more straightforward and does not require an authentic standard of metabolites for the construction of calibration curves. Additionally, the approximation in the calculation of the kinetic parameters is significantly better. Moreover, this method is easier to implement in the early stages of the drug discovery process.[56]

Furthermore, one of the metabolites detected (M1) by LC-MS corresponded to a HO-AAVPA hydroxylation product according to the observed molecular ion (252.2 m/z, Figure 4). This result was consistent with the main metabolites predicted by the SMARTCyp web server (Figure 5), which suggested that the more liable sites to undergo hydroxylation by the CYP2C9 isoform (which is homologous to rat CYP2C11) are the *meta* and *para* positions of the aryl moiety. Hence, we decided to perform the chemical synthesis of the predicted HO-AAVPA metabolites **3a** and **3b** (Scheme 2). Once the synthesis was complete, the compounds were submitted for HPLC and MS analysis to use as standards to be compared with the metabolites previously obtained by the biotransformation assay of HO-AAVPA from the rat liver microsomes. The HPLC analysis revealed that **3a** and **3b** showed approximately the same retention time as M1 (≅5.4 min, Figure 3). However, due to the low quantities of M1 obtained from the microsomal assays, complete characterization by NMR was not possible. However, these results suggest that M1 corresponds to a hydroxylated metabolite, either **3a** or **3b**.

Interaction modes between substrates and the CYP2C11 isoform were characterized by the spectral changes produced in the absorption band of Soret's peak. Type I ligands bind to the hydrophobic cavity of CYP2C11, which is located near the catalytic site. This interaction displaces a water molecule coordinated to the ferric iron (Fe^{3+}), leaving this atom pentacoordinated due to the change from a low- to a high-spin state.[15] This state favours the reduction of the haem group by electrons supplied from the NADPH via NADPH-CYP reductase, thus beginning the CYP's catalytic cycle of oxidative metabolism. Type II ligands can directly interact with Fe^{3+} as an axial ligand,[23] keeping this atom in a low-spin state. For this reason, it has been established that this type of ligand diminishes the oxidative capacity of the CYP, avoiding the reduction of the Fe^{3+} by the electrons donated by NADPH via NADPH-CYP reductase to initiate the catalytic cycle.[57] These data suggest that HO-AAVPA has affinity for the CYP2C11 isoform with an interaction mode corresponding to a type I ligand (Figure 6).

This result means that HO-AAVPA could interact directly with amino acid residues lining the cavity of the catalytic site of this CYP isoform and not as an axial ligand with the Fe atom of the haem group; thus, HO-AAVPA can be considered a CYP substrate.

In addition, through molecular docking studies, it was possible to reproduce the first part of the CYP catalytic cycle, which implies substrate binding to the enzyme; thus, it is possible to predict the affinity of HO-AAVPA for CYP2C11. Our results revealed that the binding mode of HO-AAVPA to CYP2C11 consists of the aromatic ring of HO-AAVPA oriented at an angle less than 90° to the haem group (Figure 7a), a characteristic that is consistent with other previously described aromatic substrates.[58] The predicted interactions are mainly hydrophobic, in which HO-AAVPA contacts various amino acid residues lining the haem group, and the interactions with V^{102}, I^{113}, N^{204}, F^{201}, F^{205}, F^{208}, F^{114}, E^{300}, T^{301}, L^{361}, V^{362} and L^{366} are relevant (Figure 7b).

However, despite the high-sequence homology between the CYP2C11 and CYP2C9 isoforms and the literature data suggesting that CYP2C11 could be used as a model to predict CYP2C9 activity,[59-61] the obtained results showed that there is a low probability that HO-AAVPA could be metabolized by CYP2C9 under the same mechanism observed in the CYP2C11 catalytic site.

Therefore, we have proposed a possible mechanism of HO-AAVPA biotransformation by CYP2C11, which consists of aromatic hydroxylation, as molecular simulation studies have shown that the most susceptible region for oxidative metabolism is the aromatic ring (Figures 8 and 9). This is supported by the fact that the distal hydroxyphenyl ring is oriented towards the haem group, with C-4 being the atom located in close proximity to the haem iron (Fe), so it could be expected that a hydroxyl group could be added after CYP-mediated catalysis. These results are consistent with those reported for other drugs that contain an aromatic ring in their structure. For those drugs, the formation of an arene oxide that subsequently produces a σ-cationic complex has been proposed, resulting in the formation of an oxide that will be finally converted into a hydroxyl group. In this sense, it has been shown that diclofenac follows a catalytic mechanism by CYP that is similar to the one described here, in which C-4 of the dichlorophenyl ring is in closer proximity to the Fe atom, thus producing a hydroxylated metabolite at this position.[46]

Conclusions

In this study, we combined *in silico* predictions and *in vitro* studies to investigate the CYP-mediated metabolism of HO-AAVPA. These results suggest that CYP2C11 could be mainly involved in HO-AAVPA metabolism yielding two metabolites **3a** and **3b**, whose chemical structures correspond to the hydroxylation of HO-AAVPA as was confirmed by the LC-MS analysis of the predominant metabolites yielded from *in vitro* studies with rat liver microsomes.

Declarations

Conflict of interest

The Author(s) declare(s) that they have no conflicts of interest to disclose.

Acknowledgements

Arianna Silva-Trujillo wishes to thank CONACYT for her M.Sc. scholarship (276824). The authors would like to thank to American Journal Experts (www.aje.com) for their English language revision.

Funding

This research was financially supported by CONACYT (CB254600, 782, SEP-CONACYT-ANUIES-ECOS Francia: 296636 and CB286653), ICyTDF (ICyTDF/45/2012), and COFAA-SIP/IPN (20200104/20196684/20195089).

Author's contribution

JEMW, MCRH, JCB and AA: designed the project, wrote the paper and made the discussion, AST, MB, HLMF, NLGA, FTC and ARC: developed the project either experimentally or *in silico* studies.

References

1. Devlin EJ *et al.* Cancer treatment side effects: a meta-analysis of the relationship between response expectancies and experience. *J Pain Symptom Manage* 2017; 54: 245–248.
2. Farooq M *et al.* Biological screening of novel derivatives of valproic acid for anticancer and antiangiogenic properties. *Asian Pac J Cancer Prev* 2014; 15: 7785–7792.
3. Kiang TKL *et al.* Glutathione depletion by valproic acid in sandwich-cultured rat hepatocytes: role of biotransformation and temporal relationship with onset of toxicity. *Toxicol Appl Pharmacol* 2011; 252: 318–324.
4. Pourahmad J *et al.* A new approach on valproic acid induced hepatotoxicity: involvement of lysosomal membrane leakiness and cellular proteolysis. *Toxicol In Vitro* 2012; 26: 545–551.
5. Prestegui-Martel B *et al.* N-(2-hydroxyphenyl)-2-propylpentanamide, a valproic acid aryl derivative designed in silico with improved anti-proliferative activity in HeLa, rhabdomyosarcoma and breast cancer cells. *J Enzyme Inhib Med Chem* 2016; 31(Suppl. 3): 140–149.
6. Guengerich FP. Mechanisms of cytochrome P450-catalyzed oxidations. *ACS Catal* 2018; 8: 10964–10976.
7. Sadeque AJM *et al.* Human CYP2C9 and CYP2A6 mediate formation of the hepatotoxin 4-ene-valproic acid. *J Pharmacol Exp Ther* 1997; 283: 698–703.
8. Martignoni M *et al.* Species differences between mouse, rat, dog, monkey and human CYP-mediated drug metabolism, inhibition and induction. *Expert Opin Drug Metab Toxicol* 2006; 2: 875–894.
9. Bello M *et al.* Structural and energetic analysis to provide insight residues of CYP2C9, 2C11 and 2E1 involved in valproic acid dehydrogenation selectivity. *Biochem Pharmacol* 2014; 90: 145–158.
10. Wang H *et al.* Evaluation of the binding orientations of testosterone in the active site of homology models for CYP2C11 and CYP2C13. *Biochem Pharmacol* 2009; 78: 406–413.
11. Chu V *et al.* In vitro and in vivo induction of cytochrome P450: a survey of the current practices and recommendations: a pharmaceutical research and manufacturers of America perspective. *Drug Metab Dispos* 2009; 37: 1339–1354.
12. Iber H *et al.* Regulation of hepatic cytochrome P450 2C11 by

glucocorticoids. *Arch Biochem Biophys* 1997; 345: 305–310.
13. Chang T *et al*. Selective inhibition of rat hepatic microsomal cytochrome P-450. II. Effect of the in vitro administration of cimetidine. *J Pharmacol Exp Ther* 1992; 260: 1450–1455.
14. Levine M *et al*. In vivo cimetidine inhibits hepatic CYP2C6 and CYP2C11 but not CYP1A1 in adult male rats. *J Pharmacol Exp Ther* 1998; 284: 493–499.
15. Omura T, Sato R. The carbon monoxide-binding pigment of liver microsomes. I. Evidence for its hemoprotein nature. *J Biol Chem* 1964; 239: 2370–2378.
16. Fabrizi L *et al*. Identification of the cytochrome P450 isoenzymes involved in the metabolism of diazinon in the rat liver. *J Biochem Mol Toxicol* 1999; 13: 53–61.
17. Manno M *et al*. The mechanism of the suicidal reductive inactivation of microsomal cytochrome P-450 by halothane. *Arch Toxicol* 1991; 65(3): 191–198.
18. Melet A *et al*. Substrate selectivity of human cytochrome P450 2C9: importance of residues 476, 365, and 114 in recognition of diclofenac and sulfaphenazole and in mechanism-based inactivation by tienilic acid. *Arch Biochem Biophys* 2003; 409: 80–91.
19. Khmelnitsky YL *et al*. In vitro biosynthesis, isolation, and identification of predominant metabolites of 2-(4-(2-hydroxyethoxy)-3,5-dimethylphenyl)-5,7-dimethoxyquinazolin-4(3*H*)-one (RVX-208). *Eur J Med Chem* 2013; 64: 121–128.
20. Silva-Trujillo A *et al*. A simple validated RP-HPLC bioanalytical method for the quantitative determination of a novel valproic acid arylamide derivative in rat hepatic microsomes. *Biomed Chromatogr* 2015; 29: 523–528.
21. Nath A, Atkins WM. A theoretical validation of the substrate depletion approach to determining kinetic parameters. *Drug Metab Dispos* 2006; 34: 1433–1435.
22. Cheng HC. The power issue: determination of KB or Ki from IC50. A closer look at the Cheng-Prusoff equation, the Schild plot and related power equations. *J Pharmacol Toxicol Methods* 2002; 46: 61–71.
23. Mailman RB *et al*. Effect of chemical structure on type II spectra in mouse hepatic microsomes. *Drug Metab Dispos* 1974; 2: 301–308.
24. Schenkman JB *et al*. Spectral studies of drug interaction with hepatic microsomal cytochrome. *Mol Pharmacol* 1967; 3: 113–123.
25. Kosak TM *et al*. Ether cleavage re-investigated: elucidating the mechanism of BBr 3-facilitated demethylation of aryl methyl ethers. *Eur J Org Chem* 2015; 2015: 7460–7467.
26. Sali A, Blundell TL. Comparative protein modelling by satisfaction of spatial restraints. *J Mol Biol* 1993; 234: 779–815.
27. Williams PA *et al*. Mammalian microsomal cytochrome P450 monooxygenase: structural adaptations for membrane binding and functional diversity. *Mol Cell* 2000; 5: 121–131.
28. Scott EE *et al*. Substrate routes to the buried active site may vary among cytochromes P450: mutagenesis of the F-G region in P450 2B1. *Chem Res Toxicol* 2002; 15: 1407–1413.
29. Frisch MJ *et al*. *Gaussian 98, Revision A.7*. Pittsburgh, PA: Gaussian, Inc, 1998.
30. Morris GM *et al*. Automated docking using a Lamarckian genetic algorithm and an empirical binding free energy function. *J Comput Chem* 1998; 19: 1639–1662.
31. Jo S *et al*. CHARMM-GUI Membrane Builder for mixed bilayers and its application to yeast membranes. *Biophys J* 2009; 97: 50–58.
32. Woolf TB, Roux B. Structure, energetics, and dynamics of lipid-protein interactions: a molecular dynamics study of the gramicidin A channel in a DMPC bilayer. *Proteins* 1996; 24: 92–114.
33. Woolf TB, Roux B. Molecular dynamics simulation of the gramicidin channel in a phospholipid bilayer. *Proc Natl Acad Sci U S A.* 1994; 91: 11631–11635.
34. Kaus J *et al*. Improving the efficiency of free energy calculations in the Amber Molecular Dynamics package. *J Chem Theory Comput* 2013; 9: 4131–4139.
35. Skjevik ÅA *et al*. LIPID11: a modular framework for lipid simulations using amber. *J Phys Chem B* 2012; 116: 11124–11136.
36. Wang J *et al*. Development and testing of a general Amber force field. *J Comput Chem* 2004; 25: 1157–1174.
37. Jakalian A *et al*. Fast, efficient generation of high-quality atomic charges AM1-BCC model: II. Parameterization and validation. *J Comput Chem* 2002; 23: 1623–1641.
38. Berendsen HJC *et al*. Molecular dynamics with coupling to an external bath. *J Chem Phys* 1984; 81: 3684–3690.
39. Darden T *et al*. Particle mesh Ewald: an $N\cdot\log(N)$ method for Ewald sums in large systems. *J Chem Phys* 1993; 98: 10089–10092.
40. Götz AW *et al*. Routine microsecond Molecular dynamics simulations with AMBER on GPUs. 1. Generalized born. *J Chem Theory Comput* 2012; 8: 1542–1555.
41. Salomon-Ferrer R *et al*. Routine microsecond Molecular dynamics simulations with AMBER on GPUs. 2. Explicit Solvent Particle Mesh Ewald. *J Chem Theory Comput* 2013; 9: 3878–3888.
42. van Gunsteren WF, Berendsen HJC. Algorithm for macromolecular dynamics and constraint dynamics. *Mol Phys* 1977; 34: 1311–1327.
43. Gohlke H, Case DA. Converging free energy estimates: MM-PB(GB)SA studies on the protein-protein complex Ras-Raf. *J Comput Chem* 2003; 25: 238–250.
44. Kollman PA *et al*. Calculating structures and free energies of complex molecules: combining molecular mechanics and continuum models. *Acc Chem Res* 2000; 33: 889–897.
45. Miller BR III *et al*. *MMPBSA.py*: an efficient program for end-state free energy calculations. *J Chem Theory Comput* 2012; 8: 3314–3321.
46. Yan Z *et al*. Detection of a novel reactive metabolite of diclofenac: evidence for CYP2C9-mediated bioactivation

via arene oxides. *Drug Metab Dispos* 2005; 33: 706–713.
47. Wester MR *et al.* The structure of human cytochrome P450 2C9 complexed with flurbiprofen at 2.0-Å resolution. *J Biol Chem* 2004; 279: 35630–35637.
48. Ali HI *et al.* Studies on 16-hydroxylation of steroid molecules and regioselective binding mode in homology-modeled cytochrome P450–2C11. *Int J Med Chem* 2011; 2011: 1–11.
49. Bello M *et al.* Predicting peptide vaccine candidates against H1N1 influenza virus through theoretical approaches. *Immunol Res* 2015; 62: 3–15.
50. Bello M, Correa-Basurto J. Molecular dynamics simulations to provide insights into epitopes coupled to the soluble and membrane-bound MHC-II complexes. *PLoS One* 2013; 8: e72575.
51. Wolf MG *et al.* g_membed: Efficient insertion of a membrane protein into an equilibrated lipid bilayer with minimal perturbation. *J Comput Chem* 2010; 31: 2169–2174.
52. Gerstner T *et al.* Oral valproic acid for epilepsy–long-term experience in therapy and side effects. *Expert Opin Pharmacother* 2008; 9: 285–292.
53. Hallas J *et al.* Cancer risk in long-term users of valproate: a population-based case-control study. *Cancer Epidemiol Biomarkers Prev* 2009; 18: 1714–1719.
54. Thangavel C *et al.* Inducibility of male-specific isoforms of cytochrome P450 by sex-dependent growth hormone profiles in hepatocyte cultures from male but not female rats. *Drug Metab Dispos* 2006; 34: 410–419.
55. Lee DY *et al.* Effects of enzyme inducers and inhibitors on the pharmacokinetics of intravenous torasemide in rats. *Int J Pharm* 2005; 298: 38–46.
56. Henderson CJ *et al.* An extensively humanized mouse model to predict pathways of drug disposition and drug/drug interactions, and to facilitate design of clinical trials. *Drug Metab Dispos* 2019; 47: 601–615.
57. Gan L *et al.* Role of NADPH-cytochrome P450 reductase and cytochrome-b_5/NADH-b_5 reductase in variability of CYP3A activity in human liver microsomes. *Drug Metab Dispos* 2009; 37: 90–96.
58. Masubuchi Y *et al.* Mechanism-based inactivation of CYP2C11 by diclofenac. *Drug Metab Dispos* 2001; 29: 1190–1195.
59. Lonsdale R *et al.* Quantum mechanics/molecular mechanics modeling of regioselectivity of drug metabolism in cytochrome P450 2C9. *J Am Chem Soc* 2013; 135: 8001–8015.
60. Barbosa-Sicard E *et al.* Eicosapentaenoic acid metabolism by cytochrome P450 enzymes of the CYP2C subfamily. *Biochem Biophys Res Commun* 2005; 329: 1275–1281.
61. Wang X *et al.* Pharmacokinetic interaction studies of tanshinones with tolbutamide, a model CYP2C11 probe substrate, using liver microsomes, primary hepatocytes and in vivo in the rat. *Phytomedicine* 2010; 17: 203–211.

Supporting Information

Additional Supporting Information may be found in the online version of this article:

Figure S1. (A) 1H NMR spectrum of **2a** (750 MHz, DMSO-d6). (B) 13C NMR spectrum of **2a** (188.5 MHz, DMSO-d6).

Figure S2. (A) 1H NMR spectrum of **2b** (750 MHz, DMSO-d6). (B) 13C NMR spectrum of **2b** (188.5 MHz, DMSO-d6)d.

Figure S3. (A) 1H NMR spectrum of **3a** (750 MHz, DMSO-d6). (B) 13C NMR spectrum of **3a** (188.5 MHz, DMSO-d6).

Figure S4. (A) 1H NMR spectrum of **3b** (750 MHz, DMSO-d6). (B) 13C NMR spectrum of **3b** (188.5 MHz, DMSO-d6).

Figure S5. (A) ESI/MS spectrum of **2a**. Molecular ion at 280.1913 m/z. (B) ESI/MS spectrum of **2b**. Molecular ion at 280.1903 m/z. (C) ESI/MS spectrum of **3a**. Molecular ion at 252.1595 m/z. (D) ESI/MS spectrum of **3b**. Molecular ion at 252.1596 m/z.